

Spin-orbital Yu-Shiba-Rusinov states in single Kondo molecular magnet

Received: 9 December 2021

Accepted: 13 October 2022

Published online: 27 October 2022

Check for updates

Hui-Nan Xia¹, Emi Minamitani^{2,9}, Rok Žitko^{3,4}, Zhen-Yu Liu¹, Xin Liao¹, Min Cai¹, Zi-Heng Ling¹, Wen-Hao Zhang¹, Svetlana Klyatskaya⁵, Mario Ruben^{5,6,7} & Ying-Shuang Fu^{1,8} ✉

Studies of single-spin objects are essential for designing emergent quantum states. We investigate a molecular magnet Tb_2Pc_3 interacting with a superconducting Pb(111) substrate, which hosts unprecedented Yu-Shiba-Rusinov (YSR) subgap states, dubbed spin-orbital YSR states. Upon adsorption of the molecule on Pb, the degeneracy of its lowest unoccupied molecular orbitals (LUMO) is lifted, and the lower LUMO forms a radical spin via charge transfer. This leads to Kondo screening and subgap states. Intriguingly, the YSR states display two pairs of resonances with clearly distinct behavior. The energy of the inner pair exhibits prominent inter and intra molecular variation, and it strongly depends on the tip height. The outer pair, however, shifts only slightly. As is unveiled through theoretical calculations, the two pairs of YSR states originate from the ligand spin and charge-fluctuating higher LUMO, coexisting in a single molecule, but only weakly coupled presumably due to different spatial distribution. Our work paves the way for understanding complex many-body excitations and constructing molecule-based topological superconductivity.

The exchange coupling between magnetic impurities and Bogoliubov quasiparticles of a superconductor leads to low-energy bound states inside the superconducting gap known as Yu-Shiba-Rusinov (YSR) states^{1–3}. The YSR states serve as a sensitive probe for studying intricate interactions. This capability is made possible by their sharp peak widths because of their intragap (bound state) nature that prolongs their lifetime⁴. A single spin of magnetic impurity conventionally creates a single pair of YSR states. YSR multiplet states with several pairs may also occur reflecting different interaction effects, whose origin ranges from angular momenta⁵, magnetic anisotropy⁶, magnetic exchange interactions^{7–9}, to the orbital structure of the local magnetic moment^{4,10}.

In addition to unraveling the intricate interactions, the YSR states can serve as building blocks for designing exotic emergent states. In YSR chains or lattices, their hybridization may form YSR bands of topological character, which support non-Abelian Majorana modes at the boundary^{11–15}. To date, YSR-type topological superconductors have been constructed with magnetic atoms^{16–19}. Molecular magnets hold special virtues over magnetic atoms, because of their structural stability, self-assembly capability, and chemical versatility²⁰. However, their spins are usually packaged inside spin-inactive molecular skeletons, preventing their coupling for building molecule-based topological superconductors²¹. In contrast, molecules with exposed ligand

¹School of Physics and Wuhan National High Magnetic Field Center, Huazhong University of Science and Technology, Wuhan 430074, China. ²Institute for Molecular Science, Okazaki 444-8585, Japan. ³Jožef Stefan Institute, Jamova 39, SI-1000 Ljubljana, Slovenia. ⁴Faculty of Mathematics and Physics, University of Ljubljana, Jadranska 19, SI-1000 Ljubljana, Slovenia. ⁵Institute of Nanotechnology (INT), Karlsruhe Institute of Technology (KIT), Hermann-von-Helmholtz-Platz 1, 76344 Eggenstein-Leopoldshafen, Germany. ⁶Institute for Quantum Materials and Technologies (IQMT), Karlsruhe Institute of Technology (KIT), Hermann-von-Helmholtz-Platz 1, 76344 Eggenstein-Leopoldshafen, Germany. ⁷Centre Européen de Sciences Quantiques (CESQ), Institut de Science et d'Ingénierie Supramoléculaires (ISIS), 8 allée Gaspard Monge, BP 70028, 67083 Strasbourg Cedex, France. ⁸Hubei Key Laboratory of Gravitation and Quantum Physics, Huazhong University of Science and Technology, Wuhan 430074, China. ⁹Present address: The Institute for Scientific and Industrial Research, Osaka University, Mihogaoka 8-1, Ibaraki, Osaka 567-0047, Japan. ✉e-mail: yfu@hust.edu.cn

spins are readily coupled and thereby represent excellent candidates in that regard^{22,23}. This calls for a thorough investigation of the properties of single molecular YSR states with extended ligand spins. More importantly, the ligand spins are hosted by molecular orbitals with rich textures, potentially giving rise to fundamentally new mechanism of spin-orbital entangled YSR excitations.

Here, we report an unprecedented type of YSR state, due to the interplay between a local moment and another valence-fluctuating orbital, in ligand spins of Tb_2Pc_3 molecules, phthalocyanine-based triple-decker dinuclear sandwich-type terbium complex (see Fig. 1a for its molecular structure), on superconducting Pb(111). Spectroscopic imaging scanning tunneling microscopy (SI-STM) reveals two-pair YSR states delocalized over the entire Tb_2Pc_3 . The inner YSR pair shows prominent energy evolution with changing molecule-substrate interaction, while the outer YSR pair remains nearly unshifted. First principles calculations unveil that the substrate adsorption of Tb_2Pc_3 lifts the two-fold degeneracy of its lowest unoccupied molecular orbital (LUMO) and the higher split LUMO possesses charge fluctuations. This leads to a spin-orbital correlated system, inducing two-pair YSR states, dubbed spin-orbital YSR states, that are reproduced in numerical renormalization group (NRG) simulation. Our study identifies an unexplored mechanism of inducing multiple intragap excitations, paving the way for studying coupled many-body YSR states.

Results

The measurements were performed with a custom-made Unisoku STM system (I300) at 0.4 K. Double-decker TbPc_2 molecules were deposited on Pb(111) surface at room temperature. Tb_2Pc_3 molecule contains two Tb ions sandwiched by three Pc ligands that mutually stack by 45° (Fig. 1a). TbPc_2 shares a similar structure as Tb_2Pc_3 but with one TbPc unit missing (Fig. 1a). TbPc_2 molecules self-assemble into square lattice upon surface adsorption with several sparsely imbedded brighter Tb_2Pc_3 molecules (Fig. 1b) (Supplementary Note 1). The Tb_2Pc_3 molecules are formed via a chemical reaction from TbPc_2 precursors that decompose into TbPc and Pc at a high temperature of 650–700 K in the crucible, following a reaction pathway: $4\text{TbPc}_2 \rightarrow \text{Tb}_2\text{Pc}_3 + \text{TbPc}_2 +$

$\text{TbPc} + 2\text{Pc}$ ²⁴. The formation of Tb_2Pc_3 molecules can be evidenced from its manipulation as a single entity by the STM tip (Supplementary Fig. S1a–c), as well as the existence of single decker species Pc and TbPc on the surface, whose estimated statistical ratio 1.8 is close to the value of 2 expected from the reaction pathway (Supplementary Fig. S1d, e).

Isolated TbPc_2 has a π radical spin delocalized over the two Pc ligands. The f-spin of Tb possesses high magnetic anisotropy exerted from the ligand field, but is too localized^{25,26} and plays no role in our experiments. Isolated Tb_2Pc_3 has no radical spin due to the complete pair of its π system by an additional Pc deck²⁶. The spin states of the molecules change upon substrate absorption, as determined from their low energy spectra described in the following. First, an out-of-plane field of 2 T is applied to quench the superconductivity of Pb. Tunneling spectra of TbPc_2 show featureless constant conductance at low bias. Tb_2Pc_3 molecules are classified into two types from distinct spectroscopic features (Fig. 1c). The type 1 Tb_2Pc_3 has a sharp Kondo resonance around the Fermi level E_F , as is directly evidenced from its expected Zeeman splitting (Supplementary Fig. S3)²⁷. The type 2 Tb_2Pc_3 , however, shows no Kondo resonance.

At zero magnetic field, both the TbPc_2 and the type 2 Tb_2Pc_3 display the same superconducting gaps as the Pb substrate (Fig. 1d). This indicates that the ligand spin of TbPc_2 is quenched upon adsorption²⁸, and that the type 2 Tb_2Pc_3 remains nonmagnetic. On the contrary, the type 1 Tb_2Pc_3 exhibits two pairs of sharp YSR excitations within the superconducting gap that are symmetric with respect to E_F (Fig. 1d). These subgap states are the focus of this work. The emergence of the YSR states indicates the activation of the ligand spin induced by substrate charge transfer. The nonmagnetic state in type 2 Tb_2Pc_3 suggests, instead, a negligible charge transfer.

The different charge transfer of Tb_2Pc_3 can be unraveled from the spectroscopic mapping of the TbPc_2 film at 0.5 V, showing a moiré superstructure (Supplementary Fig. S4). TbPc_2 at different moiré positions exhibit evident energy shift of the molecular orbitals (Fig. 1e). The type 1 Tb_2Pc_3 occupies the moiré region with lower conductance in Fig. 1f, whose LUMO is closer to E_F than that of the type 2 Tb_2Pc_3 by

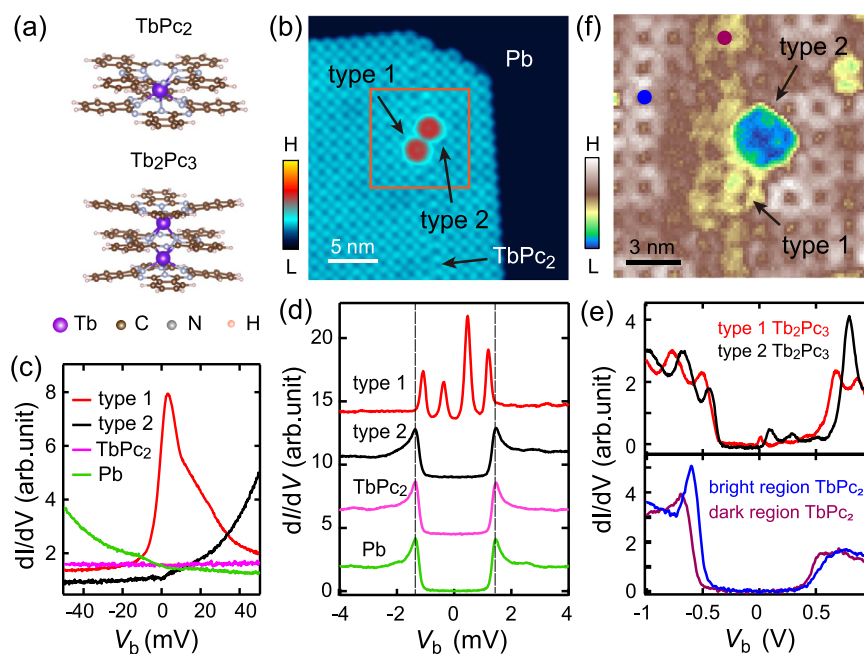


Fig. 1 | Sample morphology and molecular spin states. **a** Molecular structure of TbPc_2 and Tb_2Pc_3 . **b** STM topography ($V = -1.0$ V and $I = 10$ pA) of TbPc_2 molecular film with imbedded Tb_2Pc_3 on Pb. **c** Tunneling spectra ($V = 50$ mV, $I = 100$ pA) of Tb_2Pc_3 under 2 T. **d** High-energy resolution spectra ($V = 10$ mV and $I = 100$ pA) of Pb

substrate, TbPc_2 and the two types of Tb_2Pc_3 . The dashed lines mark the energy of the superconducting coherence peaks. **e** Tunneling spectra ($V = 1.0$ V and $I = 100$ pA) showing electronic structure of Tb_2Pc_3 and TbPc_2 at different moiré regions. **f** dI/dV mapping ($V = 615$ mV, $I = 100$ pA) of the rectangle area in (b).

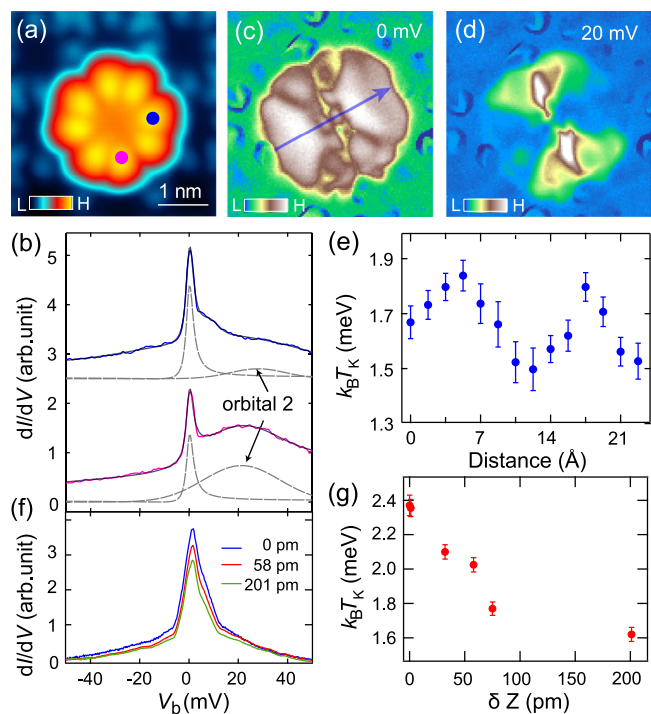


Fig. 2 | Kondo effect of Tb_2Pc_3 . **a** STM image ($V = -1.0$ V and $I = 10$ pA) of an imbedded type-1 Tb_2Pc_3 . **b** Tunneling spectra ($V = 50$ mV and $I = 100$ pA) taken at locations indicated in **(a)** at 2 T, showing Kondo resonances and the upper LUMO. The fitting curves are shown in gray. **c**, **d** dI/dV mapping of **(a)** taken at the indicated energies. **e** Variation of the resonance width extracted from the spectra taken along the blue arrow in **(c)**. **f** Tunneling spectra taken at the same location of a Tb_2Pc_3 , showing evolution of the Kondo resonance with decreasing tip height δZ , where $\delta Z = 0$ pm is set at $V = 5$ mV and $I = 50$ pA. **g** The Kondo peak width extracted from **(a)** as a function of δZ .

-100 meV (Fig. 1e). This demonstrates the moiré modulation of molecule-substrate interaction²⁹, resulting in the different charge transfer to Tb_2Pc_3 . The graphene substrate has no effect on the charge transfer process, because its carrier density is negligible compared to that of Pb.

Similar to $TbPc_2$, the STM image of Tb_2Pc_3 displays an eight-lobed structure corresponding to its top Pc (Fig. 2a). Spectra measured over all the lobes exhibit a Kondo resonance, conforming to the delocalized ligand spin (Fig. 2b). Notably, its LUMO appears at -20 meV. The LUMO intensity anti-correlates with that of the Kondo resonance (Fig. 2b), as is more explicitly seen from the spectroscopic mapping at 20 and 0 mV, respectively (Fig. 2c, d). Surprisingly, the spatial symmetry of both mappings reduces to two-fold, in apparent conflict with the four-fold symmetry of free Tb_2Pc_3 , suggesting the essential role of substrate coupling. For the type 1 Tb_2Pc_3 , their different embedded positions in the moiré pattern result in the variations in their LUMO energies and the Kondo temperatures, due to the different coupling strength to the substrate. The Kondo peak width, as extracted from the Fano fitting (Supplementary Fig. S5), varies from 1 to 3 meV for different molecules. The Kondo temperature becomes higher when the LUMO is closer to E_F , in line with the theoretical expectation³⁰.

Moreover, within a single Tb_2Pc_3 the Kondo resonance width exhibits prominent intramolecular variation (Fig. 2e), even though the width is expected to be uniform across the molecule. The variation is most likely a tip effect: the force between the STM tip and the molecule changes the molecule-substrate coupling strength and the magnitude of this effect depends on the lateral position of the tip. This scenario is indeed justified from the decrease of the resonance width at smaller tip height (Fig. 2f, g), which demonstrates that the tip-molecule

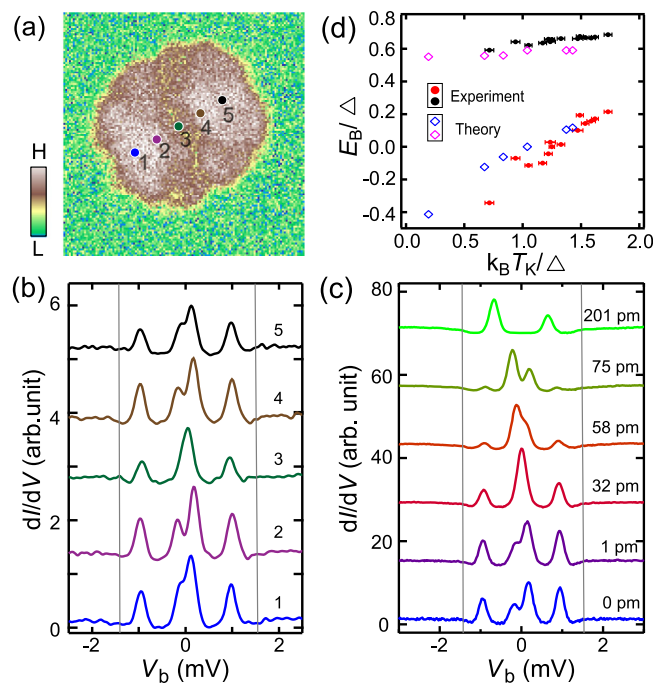


Fig. 3 | YSR state of Tb_2Pc_3 . **a** dI/dV mapping of the Tb_2Pc_3 in Fig. 2a at 0.3 mV, showing the intensity distribution of the YSR state. **b** Selective spectra ($V = 10$ mV and $I = 100$ pA) taken at the indicated positions in **(a)**. The gray lines depict the energies of the superconducting coherence peaks of Pb. **c** Variation of YSR states taken at the same location of a Tb_2Pc_3 with decreasing tip height δZ . The $\delta Z = 0$ pm value is set at $V = 10$ mV and $I = 50$ pA. **d** Statistics showing the relation between E_B and T_K relative to the Pb superconducting gap Δ . Black (red) solid dots are experimental outer (inner) YSR state. Pink (blue) hollow dots are theoretically calculated outer (inner) YSR states.

interaction lifts the molecule away from the substrate, reducing the molecule-substrate coupling, as observed in related systems^{31,32}. Similar effect of the tip force has also been observed on an oxygen-up VOPc molecule, whose interaction with the Pb substrate becomes enhanced with decreasing tip height, inducing quantum phase transition of the associated YSR state³³.

Since Kondo screening competes with the superconducting pairing^{21,33,34}, the tip-position dependent Kondo coupling provides a way of studying such competing ground states within a single molecule. As shown in Fig. 1d, the YSR states of the type 1 Tb_2Pc_3 taken at the indicated lobe (Fig. 2a, blue dot) exhibit two prominent YSR pairs located at ± 0.48 and ± 1.2 meV, respectively. The superconducting coherence peaks on the Kondo molecule are absent due to the transfer of the spectral weight to these subgap states. There is a sizeable asymmetry in the intensity of the YSR states, with a ratio between the hole and electron components of 2.73 (1.43) for the inner (outer) YSR pair. This asymmetry is caused by the non-integer filling of the orbitals which is equivalent to potential scattering.

To unveil the spatial distribution of the YSR states, we performed spectroscopic mapping of the molecule at 0.3 mV, corresponding to the hole component of the inner YSR pair. Interestingly, the YSR state intensity also exhibits a two-fold symmetry (Fig. 3a), similar to that of the Kondo resonance, indicating the common origin of the two features. Figure 3b shows a series of spectra measured along the molecule. The inner and outer YSR pairs are shifted, but in very different ways, both in the amplitude and the direction of the shift. Specifically, the inner (outer) YSR pair shifts nonmonotonically (monotonically) towards E_F with the spectroscopic locations moving from the edge of the molecule to its center. The inner YSR pair has a much larger energy shift of 0.2 meV than that of the outer YSR pair, i.e., 0.06 meV. Similar

behavior exists in other molecules with different Kondo temperatures (Supplementary Fig. S6). More interestingly, the YSR states can be manipulated via changing the tip-sample separation δZ . As is shown in Fig. 3c, with reducing δZ , the inner YSR state exhibits even larger intramolecular shift, to the point that the states cross E_F which indicates a quantum phase transition. At the same time, the outer YSR pair stays almost unshifted. This demonstrates that changing δZ can effectively tune the strength of the molecule-substrate coupling, conforming to the variation of T_K shown in Fig. 2e, g.

The YSR energy evolves with the Kondo coupling strength, as parametrized by the Kondo temperature T_K . The strength of the Kondo coupling T_K relative to the superconducting gap Δ determines whether the ground state is a Kondo-like singlet or a free-spin-like doublet with a quantum phase transition at $T_K \sim 0.3\Delta$ for spin $S = 1/2$ systems^{34,35}. We have collected the statistics on the inner YSR energy and the Kondo temperature scaled by the superconducting gap Δ on different molecules imbedded inside the TbPc₂ films in conjunction with the intramolecular variation. As shown in Fig. 3d, their relation collapses onto the same curve. Namely, the inner YSR state monotonically shifts from negative energy to positive energy with increasing T_K with a quantum phase transition at $T_K \sim 1.26\Delta$. The transition point is larger than that of a conventional spin 1/2 system, calling for future theoretical understanding. On the other hand, the binding energy of the outer YSR state merely slightly increases with increasing T_K .

To unravel the origin of the two-pair YSR states, we carried out density functional theory (DFT) plus U calculations³⁶ for Tb₂Pc₃ on Pb(111) with the adsorption configuration shown in Fig. 4a. Such

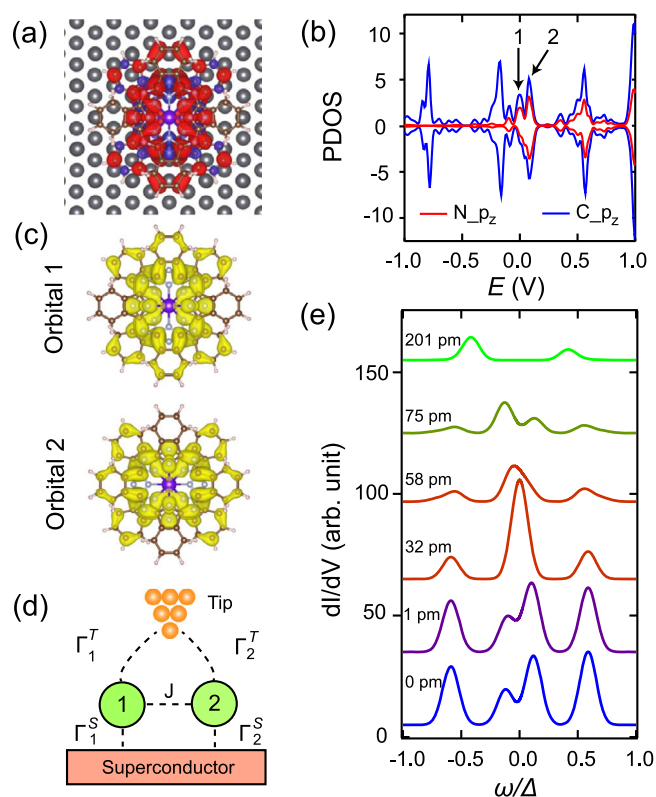


Fig. 4 | Theoretical calculations. **a** DFT calculated spatial distribution of magnetic moment in Tb₂Pc₃ on Pb(111) (gray balls). The red (blue) color represents spin-up (spin-down) electron density. **b** PDOS of Tb₂Pc₃ on Pb(111) projected on p_z orbital of C and N atoms. Orbital 1 and orbital 2 are split due to adsorption on Pb(111). **c** Charge distribution of the two orbitals in isolated [Tb₂Pc₃], which correspond to the orbitals marked with arrows in (b). **d** Schematics showing the theoretical model. The two orbitals 1 and 2 couple to each other with the exchange coupling J , while Γ_i^T (Γ_i^S) represents the hybridization between the orbital $i = 1, 2$ and the tip (superconducting substrate). **e** Calculated variation of YSR states by reducing tip height δZ .

configuration conforms to that of an isolated Tb₂Pc₃ determined experimentally (Supplementary Fig. S7), which displays a Kondo resonance and thus is representative of the type 1 Tb₂Pc₃. After structure optimization, the total magnetic moment of the molecule is $0.38\mu_B$, demonstrating charge transfer to the LUMO from the substrate, as is also supported from the differential charge distribution (Supplementary Fig. S8). The spatial distribution of the magnetic moment (Fig. 4a) matches that of the Kondo peak. The adsorption induces molecular distortion, lifting the doubly degenerated LUMO and reducing their symmetry from four-fold to two-fold. From the comparison of the DOS projected on the p_z orbitals of C and N atoms (Fig. 4b) with that of the isolated [Tb₂Pc₃]⁻ (Supplementary Fig. S9), we assign the two peaks marked with black arrows in Fig. 4b to the degeneracy-lifted LUMO, whose spatial distributions are shown in Fig. 4c. Evidently, orbital 1 of the lower LUMO resembles nicely with that of the spin distribution in Fig. 4a, demonstrating it hosts the ligand spin. Orbital 2 partially overlaps with E_F , putting it in the valence fluctuation regime.

The situation in this molecule resembles that in double quantum dots connected to superconductor leads, where two pairs of YSR states have been predicted³⁷. Therefore, we model the YSR states with the orbital splitting based on the following Hamiltonian:

$$H = \sum_{koi} \varepsilon_k c_{koi}^\dagger c_{koi} + \sum_{ki} \Delta (c_{k\uparrow i}^\dagger c_{-k\downarrow i}^\dagger + h.c.) + \sum_{io} \varepsilon_i d_{io}^\dagger d_{io} + \sum_i U_i n_{i\uparrow} n_{i\downarrow} + \left(\sum_{iko} V_i d_{io}^\dagger c_{koi} + h.c. \right) - JS_1 \cdot S_2 \quad (1)$$

Here the first two terms represent the BCS superconducting state of Pb. The third and fourth terms represent the two ($i = 1, 2$) ligand orbitals of Tb₂Pc₃. The fifth term is the hybridization between the molecular orbitals and the Pb substrate, where the hybridization strength is $\Gamma_i^S = \pi V_i^2 \rho_i$. The final term corresponds to the coupling between the spins in the two orbitals. Other notations are standard. The STM tip height determines the substrate-molecule and molecule-tip distances. The hybridization of the molecular orbitals with the tip is much smaller than that with the substrate, $\Gamma_i^T \ll \Gamma_i^S$, thus the YSR energies are determined by Γ_i^S , while Γ_i^T determines the contribution of both orbitals to the total tunneling current, which is calculated via Bardeen's approach from the orbital spectral functions. The model is schematically shown in Fig. 4d. The impurity problem is solved using the NRG method^{38,39}. In this model, the ratios Γ_i^S/U_i governs the physical properties. We consider the situation in which the 1st orbital is in the local-moment regime with $U_1/\pi\Gamma_1^S > 1$, and the 2nd orbital in the valence-fluctuation regime with $U_2/\pi\Gamma_2^S < 1$. While the spin in a valence-fluctuating orbital is not well defined, it still creates YSR states⁴⁰⁻⁴³, because of its wavefunction component with single electron occupancy. The calculations were performed in the wide-band limit for parameters $U_1/\Delta = 100$, $U_2/\Delta = 10$, $\varepsilon_1/\Delta = -25$, $\varepsilon_2/\Delta = -4$, with fixed large hybridization for $\Gamma_2^S/U_2 = 0.375$ and variable hybridization for Γ_1^S/U_1 in the range 0.06–0.092. Furthermore, we set $J/U_1 = -0.005$, which corresponds to a weak yet non-negligible Hund's coupling, presumably due to the nearly orthogonal symmetry of the two LUMO states. We assume that both Γ_1^S and Γ_2^T exponentially depend on Z , i.e., $\Gamma_1^S \sim e^{-\kappa_1^S Z}$ and $\Gamma_2^T \sim e^{-\kappa_2^T Z}$, and that $\kappa_2^T/\kappa_1^S = 12$. This empirical model is based on the measured dI/dV data, showing variation of inner peak positions, while the outer peak positions are nearly constant. The simulation results shown in Fig. 4e reproduce the measurements from Fig. 3c rather well, supporting our model. This indicates that the valence-fluctuating orbital experiences inter-orbital coupling to the local moment, and the inner (outer) YSR pair originates from spin (orbital), because it closely (slightly) evolves with the changing Kondo temperature. As such, this new type of YSR excitation is dubbed as spin-orbital YSR state. The spin-orbital YSR state should be generic to molecules experiencing orbital degeneracy lifting and charge transfer

upon substrate adsorption. The simulation also highlights the dual role of the tip height in this system, affecting either molecule-substrate or molecule-tip coupling for either orbital.

It is noted that our model is formally similar to that of ref. 8, but the parameter regime is entirely different. In the case of ref. 8, the two orbitals strongly couple into a $S=1$ collective state, resulting in identical particle-hole intensity pattern in their two YSR pairs. In contrast, our case is in the regime of two weakly coupled levels, whose associated two YSR pairs may exhibit different particle-hole asymmetry. Our study indicates that valence fluctuations can suppress the effect of exchange coupling between the spin channels within the same molecular structure, which is a priori expected to be usually strong.

In summary, we have investigated the two-pair YSR states in Tb_2Pc_3 on Pb (111). The LUMO of Tb_2Pc_3 gets singly occupied upon adsorption on Pb, and experiences orbital degeneracy lifting. The ligand spin induces Kondo screening and YSR subgap states in the Pb host. The orbital splitting of the LUMO and its charge fluctuation results in two pairs of YSR states, corresponding to a weakly-coupled two-impurity YSR system in a single molecule. Similar YSR state has also been observed in Y_2Pc_3 , confirming the negligible influence of the f-moment on the ligand spin state, in agreement with DFT calculations on Tb_2Pc_3 with full f-electrons plus U (Supplementary Note 2). Our work identifies a new category of spin-orbital YSR state, which permits a study of spin physics in a multi-level molecule that would otherwise be difficult to spectrally resolve and may aid the understanding of more complex many-body excitations. In view of the delocalized nature of the ligand spin, this also paves the way for tailoring magnetically coupled molecular structures for realizing topological superconductivity.

Methods

Experiments

The experiments were carried out with a custom-designed Unisoku STM (I300) at 0.4 K. The detailed procedures for preparing the graphene covered SiC(0001) substrate have been reported in ref. 44. The Pb mesa is grown on the graphene substrate at room temperature. The thickness of the grown Pb islands is typically about 5 nm, whose superconducting gap size at 0.4 K is measured as about 1.35 meV (Supplementary Fig. S10), which is close to the bulk value and also conforms to the previous study⁴⁵. TbPc_2 molecules are evaporated onto the Pb surface at room temperature. An electro-etched W wire was used as the STM probe, which had been cleaned and characterized on a Cu(111) crystal prior to the measurement. The dI/dV spectra were acquired using conventional lock-in technique with a bias modulation of 1 mV and 50 μV at 983 Hz for the detection of Kondo peaks and YSR states, respectively.

Theory

The DFT calculations are carried out by Vienna ab-initio simulation (VASP) package^{46,47} with the projected augmented wave (PAW) method⁴⁸. Exchange-correlation functional with non-local correction via van-der Waals interaction developed by Hamada⁴⁹ were used. VASPkit package⁵⁰ was used to analyze the DOS calculation data. The molecular structures, charge densities, and spin distributions are visualized by VESTA⁵¹. The Pb substrate is modeled by 4-layer thickness slab with the supercell size of (8×8). To stabilize the ligand spin, we employ $U=4.5$ eV and $J=1.0$ eV on p -orbitals of N and C atoms. We used pseudopotential of Tb(III) ion in VASP with a fixed f-electron state, which is a standard method for assessing the ligand electronic state of the phthalocyanine complex⁵². This treatment is rationalized by additional calculations on Tb_2Pc_3 using full f-electrons plus U , which deliver similar electronic states of molecular levels as the fixed f-electron pseudopotential (Supplementary Note 2). This conforms to the strong localization of Tb f-electrons in the phthalocyanine complex, which makes the interaction between f- and π -electrons weak^{53,54}.

In the calculations of Tb_2Pc_3 on Pb(111), the initial guess of the magnetic moment for all the carbon and nitrogen atom was set to 0.1 μ_B (in total 12.0 μ_B). Therefore, the obtained solution was started from a state without time-reversal symmetry. We carried out electronic and structure relaxation without any constraint on the magnetic state. Thus, our calculation reflects the ground state. Due to the structural symmetry breaking of Tb_2Pc_3 on Pb(111), one of the LUMO orbitals possesses the unpaired electron, and the other orbital has much smaller occupation. The AFM coupling between the two orbitals in Tb_2Pc_3 on Pb(111) could be seen from the spin density for the majority and minority spin components in Supplementary Fig. S11. The minority spin component is orthogonal to, and smaller than, the majority spin component. Considering that the two LUMO orbitals are orthogonal, this suggests that the first (second) LUMO orbital is occupied by majority (minority) spin, and consequently there is AFM coupling between the two orbitals. We note that the Pb(111) substrate plays an important role to form the AFM coupling, and the magnetic coupling in an isolated Tb_2Pc_3 may be different.

The NRG calculations were performed with the NRG Ljubljana package (<https://github.com/rozkztko/nrgljublana>). The discretization parameter was $\Lambda=4$, we kept up to 5000 multiplets (the sole conserved quantum number was the total spin S), or cutoff 9 in units of the current NRG scale. The subgap part of the spectral functions was broadened using Gaussian kernels with width $\Delta/10$, thereby mimicking the experimental broadening due to finite temperature and electromagnetic noise. The tunneling current is simulated via Bardeen's tunneling approach:

$$I = 4\pi e/\hbar \sum_{i=1}^2 \int_0^{eV} \rho_{S,i}(\mu - eV + \delta\epsilon) \rho_T(\mu + \delta) |M_i|^2 d\delta.$$

Here the sum runs over the two molecular orbitals that contribute most current in the subgap region; we assumed that there is no interference between the two contributions. V is the bias voltage, $\rho_{S,i}$ is the spectral function of the orbital i (computed using the NRG solver), ρ_T is the tip spectral function (assumed constant in energy), and M_i is the tunneling matrix element between the tip and the molecular orbital i . These matrix elements are proportional to the tip hybridization function Γ_i^T (see Fig. 4d for a schematic representations of the couplings) and we assume them to be constant in energy. We furthermore assume that the hybridizations Γ_1^S and Γ_2^T depend exponentially on the tip position, as in $\Gamma_1^S = \Gamma_1^S(0) \exp[-\kappa_1^S(Z - Z_0)]$ and $\Gamma_2^T = \Gamma_2^T(0) \exp[-\kappa_2^T(Z - Z_0)]$, while other hybridizations do not depend on Z . We find that good agreement with the experimental measurements is obtained for $\kappa_2^T/\kappa_1^S = 12$.

Molecule synthesis

Synthesis of TbPc_2 is accomplished by direct cyclization of the ring pre-cursor (1,2-dicyanobenzene) at high temperatures in the presence of a metal salt (e.g., $\text{Tb}(\text{acac})_3$), 1,8-diazabicyclo (5.4.0) undec-7-ene (DBU) and high boiling solvents (e.g., penthanol, hexanol)⁵⁵.

Data availability

All data needed to evaluate the conclusions in the paper are present in the paper and the Supplementary Information. Additional data related to this paper may be requested from the authors.

Code availability

The code that supports the findings of this study is available from the corresponding author upon reasonable request.

References

1. Yu, L. Bound state in superconductors with paramagnetic impurities. *Acta Phys. Sin.* **21**, 75–91 (1965).

2. Shiba, H. Classical spins in superconductors. *Prog. Theor. Phys.* **40**, 435–451 (1968).
3. Rusinov, A. I. On the theory of gapless superconductivity in alloys containing paramagnetic impurities. *Zh. Eksp. Teor. Fiz.* **56**, 2047–2056 (1969).
4. Choi, D.-J. et al. Mapping the orbital structure of impurity bound states in a superconductor. *Nat. Commun.* **8**, 15175 (2017).
5. Ji, S. H. et al. High-resolution scanning tunneling spectroscopy of magnetic impurity induced bound states in the superconducting gap of Pb thin films. *Phys. Rev. Lett.* **100**, 226801 (2008).
6. Hatter, N. et al. Magnetic anisotropy in Shiba bound states across a quantum phase transition. *Nat. Commun.* **6**, 8988 (2015).
7. Shawlienu, K. et al. Coupled Yu-Shiba-Rusinov states in molecular dimers on NbSe₂. *Nano Lett.* **18**, 2311–2315 (2018).
8. Rubio-Verdú, C., Zaldívar, J., Žitko, R. & Pascual, J. I. Coupled Yu-Shiba-Rusinov states induced by a many-body molecular spin on a superconductor. *Phys. Rev. Lett.* **126**, 017001 (2021).
9. Beck, P. et al. Spin-orbit coupling induced splitting of Yu-Shiba-Rusinov states in antiferromagnetic dimers. *Nat. Commun.* **12**, 2040 (2021).
10. Ruby, M. et al. Orbital picture of Yu-Shiba-Rusinov multiplets. *Phys. Rev. Lett.* **117**, 186801 (2016).
11. Pientka, F., Glazman, L. I. & von Oppen, F. Topological superconducting phase in helical Shiba chains. *Phys. Rev. B* **88**, 155420 (2013).
12. Klinovaja, J. et al. Topological superconductivity and Majorana fermions in RKKY systems. *Phys. Rev. Lett.* **111**, 186805 (2013).
13. Röntynen, J. & Ojanen, T. Topological superconductivity and high Chern numbers in 2D ferromagnetic Shiba lattices. *Phys. Rev. Lett.* **114**, 236803 (2015).
14. Li, J. et al. Two-dimensional chiral topological superconductivity in Shiba lattices. *Nat. Commun.* **7**, 12297 (2016).
15. Sato, M. & Ando, Y. Topological superconductors: A review. *Rep. Prog. Phys.* **80**, 076501 (2017).
16. Nadj-Perge, S. et al. Observation of Majorana fermions in ferromagnetic atomic chains on a superconductor. *Science* **346**, 602–607 (2014).
17. Ménard, G. C. et al. Two-dimensional topological superconductivity in Pb/Co/Si(111). *Nat. Commun.* **8**, 2040 (2017).
18. Palacio-Morales, A. et al. Atomic-scale interface engineering of Majorana edge modes in a 2D magnet-superconductor hybrid system. *Sci. Adv.* **5**, eaav6600 (2019).
19. Schneider, L. et al. Topological Shiba bands in artificial spin chains on superconductors. *Nat. Phys.* **17**, 943–948 (2021).
20. Coronado, E. Molecular magnetism: from chemical design to spin control in molecules, materials, and devices. *Nat. Rev. Mater.* **5**, 87–104 (2020).
21. Franke, K. J. et al. Competition of superconducting phenomena and Kondo screening at the nanoscale. *Science* **332**, 940–944 (2011).
22. Amokrane, A. et al. Role of pi-radicals in the spin connectivity of clusters and networks of Tb double-decker single molecule magnets. *ACS Nano* **11**, 10750–10760 (2017).
23. Karan, S. et al. Spin manipulation by creation of single-molecule radical cations. *Phys. Rev. Lett.* **116**, 027201 (2016).
24. Hellerstedt, J. et al. On-surface structural and electronic properties of spontaneously formed Tb₂Pc₃ single molecule magnets. *Nanoscale* **10**, 15553–15563 (2018).
25. Fu, Y. S. et al. Reversible chiral switching of bis(phthalocyaninato) terbium(III) on a metal surface. *Nano Lett.* **12**, 3931–3935 (2012).
26. Komeda, T. et al. Observation and electric current control of a local spin in a single-molecule magnet. *Nat. Commun.* **2**, 217 (2011).
27. Fu, Y. S. et al. Manipulating the Kondo resonance through quantum size effects. *Phys. Rev. Lett.* **99**, 256601 (2007).
28. Chen, X. et al. Probing superexchange interaction in molecular magnets by spin-flip spectroscopy and microscopy. *Phys. Rev. Lett.* **101**, 197208 (2008).
29. Ji, S. H. et al. Kondo effect in self-assembled manganese phthalocyanine monolayer on Pb islands. *Chin. Phys. Lett.* **27**, 087202 (2010).
30. Hewson, A. C. *The Kondo Problem to Heavy Fermions* (Cambridge University Press, 1993).
31. Farinacci, L. et al. Tuning the coupling of an individual magnetic impurity to a superconductor: Quantum phase transition and transport. *Phys. Rev. Lett.* **121**, 196803 (2018).
32. Huang, H. et al. Quantum phase transitions and the role of impurity-substrate hybridization in Yu-Shiba-Rusinov states. *Commun. Phys.* **3**, 199 (2020).
33. Malavolti, L. et al. Tunable spin-superconductor coupling of spin 1/2 vanadyl phthalocyanine molecules. *Nano Lett.* **18**, 7955–7961 (2018).
34. Matsuura, T. et al. The effects of impurities on superconductors with Kondo effect. *Prog. Theor. Phys.* **57**, 1823–1835 (1977).
35. Balatsky, A. V. et al. Impurity-induced states in conventional and unconventional superconductors. *Rev. Mod. Phys.* **78**, 373–433 (2006).
36. Peters, R. et al. Numerical renormalization group approach to Green's functions for quantum impurity models. *Phys. Rev. B* **74**, 245114 (2006).
37. Žitko, R. Numerical subgap spectroscopy of double quantum dots coupled to superconductors. *Phys. Rev. B* **91**, 165116 (2015).
38. Ralf, B. et al. Numerical renormalization group method for quantum impurity systems. *Rev. Mod. Phys.* **80**, 395 (2008).
39. Bauer, J. et al. Spectral properties of locally correlated electrons in a Bardeen-Cooper-Schrieffer superconductor. *J. Phys.: Condens. Matter* **19**, 486211 (2007).
40. Yoshioka, T. & Ohashi, Y. Numerical renormalization group studies on single impurity anderson model in superconductivity: A unified treatment of magnetic, nonmagnetic impurities, and resonance scattering. *J. Phys. Soc. Jpn.* **69**, 1812–1823 (2000).
41. Pillet, J. D. et al. Andreev bound states in supercurrent-carrying carbon nanotubes revealed. *Nat. Phys.* **6**, 965–969 (2010).
42. Pillet, J. D., Joyez, P., Žitko, R. & Goffman, M. F. Tunneling spectroscopy of a single quantum dot coupled to a superconductor: From Kondo ridge to Andreev bound states. *Phys. Rev. B* **88**, 045101 (2013).
43. Lee, E. J. H. et al. Scaling of subgap excitations in a superconductor-semiconductor nanowire quantum dot. *Phys. Rev. B* **95**, 180502(R) (2017).
44. Yang, X. et al. Possible Phason-polarons in purely one-dimensional charge order of Mo₆Se₆ nanowires. *Phys. Rev. X* **10**, 031061 (2020).
45. Paschke, F. et al. Hydrogen-intercalated graphene on SiC as platform for hybrid superconductor devices. *Adv. Quantum Technol.* **3**, 2000082 (2020).
46. Kresse, G. et al. Efficient iterative schemes for ab initio total-energy calculations using a plane-wave basis set. *Phys. Rev. B* **54**, 11169 (1996).
47. Kresse, G. et al. Efficiency of ab-initio total energy calculations for metals and semiconductors using a plane-wave basis set. *Comput. Mater. Sci.* **6**, 15 (1996).
48. Blöchl, P. E. Projector augmented-wave method. *Phys. Rev. B* **50**, 17953 (1994).
49. Hamada, I. Van der Waals density functional made accurate. *Phys. Rev. B* **89**, 121103(R) (2014).
50. Wang, V. et al. VASPKit: A user-friendly interface facilitating high-throughput computing and analysis using VASP code. *Comput. Phys. Commun.* **267**, 108033 (2021).

51. Momma, K. & Izumi, F. VESTA 3 for three-dimensional visualization of crystal, volumetric and morphology data. *J. Appl. Crystallogr.* **44**, 1272–1276 (2011).
52. Shahed, S. M. F. et al. Observation of Yu–Shiba–Rusinov states and inelastic tunneling spectroscopy for intramolecule magnetic exchange interaction energy of terbium phthalocyanine (TbPc) species adsorbed on superconductor NbSe₂. *ACS Nano* **16**, 7651–7661 (2022).
53. Vitali, L. et al. Electronic structure of surface-supported Bis(phthalocyaninato) terbium(III) single molecular magnets. *Nano Lett.* **8**, 3364–3368 (2008).
54. Vruble, I. I. et al. An ab initio perspective on scanning tunneling microscopy measurements of the tunable Kondo resonance of the TbPc₂ molecule on a gold substrate. *Phys. Rev. B* **101**, 125106 (2020).
55. Stepanow, S. et al. Spin and orbital magnetic moment anisotropies of monodispersed bis(Phthalocyaninato) terbium on a copper surface. *J. Am. Chem. Soc.* **132**, 11900–11901 (2010).

Acknowledgements

We thank Prof. Michal Otepka, Prof. Pavel Jelinek, and Prof. Guoying Gao for helpful discussions. This work was funded by the National Key Research and Development Program of China (Grant Nos. 2017YFA0403501, 2018YFA0307000), the National Natural Science Foundation of China (Grant Nos. U20A6002, 11874161, and 11774105). R.Ž. acknowledges the support of the Slovenian Research Agency (ARRS) under P1-0044 and P1-0416. DFT calculations were performed using a computer facility at the Research Center for Computational Science (Okazaki, Japan).

Author contributions

H.N.X., Z.Y.L., and X.L. did the experiments with the help of M.C., Z.H.L., and W.H.Z.; E.M. did the DFT calculations; R.Z. did the NRG modeling; S.K. and M.R. synthesized the molecule; Y.S.F., H.N.X., E.M., R.Z., and M.R. analyzed the data and wrote the manuscript with comments from all authors. Y.S.F. supervised the project.

Competing interests

The authors declare no competing interests.

Additional information

Supplementary information The online version contains supplementary material available at <https://doi.org/10.1038/s41467-022-34187-8>.

Correspondence and requests for materials should be addressed to Ying-Shuang Fu.

Peer review information *Nature Communications* thanks the anonymous reviewer(s) for their contribution to the peer review of this work. Peer reviewer reports are available.

Reprints and permissions information is available at <http://www.nature.com/reprints>

Publisher's note Springer Nature remains neutral with regard to jurisdictional claims in published maps and institutional affiliations.

Open Access This article is licensed under a Creative Commons Attribution 4.0 International License, which permits use, sharing, adaptation, distribution and reproduction in any medium or format, as long as you give appropriate credit to the original author(s) and the source, provide a link to the Creative Commons license, and indicate if changes were made. The images or other third party material in this article are included in the article's Creative Commons license, unless indicated otherwise in a credit line to the material. If material is not included in the article's Creative Commons license and your intended use is not permitted by statutory regulation or exceeds the permitted use, you will need to obtain permission directly from the copyright holder. To view a copy of this license, visit <http://creativecommons.org/licenses/by/4.0/>.

© The Author(s) 2022